Helicity Evolution in Emerging Active Regions

Alexei A. Pevtsov

National Solar Observatory[1] */Sacramento Peak, Sunspot, NM 88349, U.S.A.*

apevtsov@nso.edu

Vasily M. Maleev

NSO 2002 Summer Research Assistant from Saint Petersburg State University, Petrodvorets, Saint Petersburg, Russia

vasya@astro.spbu.ru

and

Dana W. Longcope

Department of Physics, Montana State University, Bozeman, MT 59717-3840, U.S.A.

dana@physics.montana.edu

ABSTRACT

We study the evolution of twist and magnetic helicity in the coronal fields of active regions as they emerge. We use multi-day sequences of SoHO MDI magnetograms to characterize the region's emergence. We quantify the overall twist in the coronal field, α, by matching a linear force-free field to bright coronal structures in EUV images. At the beginning of emergence all regions studied have $\alpha \simeq 0$. As the active region grows, α increases and reaches a plateau within approximately one day of emergence. The inferred helicity transport rate is larger than differential rotation could produce. Following Longcope & Welsch (2000) we develop a model for the injection of helicity into the corona by the emergence of a twisted flux tube. This model predicts a ramp-up period of approximately one day. The observed time-history $\alpha(t)$ is fit by this model assuming reasonable values for the sub-photospheric Alfvén speed. The implication is that helicity is carried by twisted flux tubes rising from the convection zone, and transported across the photosphere by spinning of the poles driven by magnetic torque.

Subject headings: Sun: magnetic fields; sunspots — Sun: corona

---

[1]National Solar Observatory (NSO) is operated by the Association of Universities for Research in Astronomy Inc. (AURA) under cooperative agreement with the National Science Foundation.

1. Introduction

It is widely accepted now that the magnetic field of active regions is generated by the dynamo operating at the bottom of the convection zone. The dynamo flows transfer their kinetic helicity ($H_k = \int(\nabla \times \mathbf{v}) \cdot \mathbf{v} dD$) into magnetic field helicity (magnetic, $H_m = \int(\nabla \times \mathbf{A}) \cdot \mathbf{B} dD$ or current, $H_c = \int(\nabla \times \mathbf{B}) \cdot \mathbf{B} dD$, where $\mathbf{A}, \mathbf{B}, \mathbf{v}$ are magnetic vector potential, magnetic induction and velocity, accordingly). Once magnetic field crosses the photosphere, helicity manifests itself via non-zero twist or electric currents. Indeed, most, if not all, active regions exhibit some degree of twist in their photospheric magnetic fields (e.g., Pevtsov, Canfield, & Metcalf 1995; Bao & Zhang 1998). Some of these electric currents should propagate up into the corona, as the observations show a good correlation between photospheric and coronal force-free field α coefficient (Pevtsov, Canfield, & McClymont 1997; Burnette, Canfield, & Pevtsov 2003). The twist observed in the photosphere may be of sub-photospheric origin (e.g., Longcope et al. 1999) or due to (near) surface motions (e.g., differential rotation/shear motions, DeVore 2000; Chae 2001). Numerical simulations have established that a small amount of twist is necessary for a flux tube rising through the convection zone to survive as an entity (Emonet & Moreno-Insertis 1998; Fan, Zweibel, & Lantz 1998). Observations also indicate that magnetic field emerges carrying non-zero twist (Leka et al. 1996; Portier-Fozzani et al. 2001; Grigoryev & Ermakova 2002), which implies that at least some fraction of photospheric helicity may be generated below the photosphere.

Berger & Field (1984) showed that magnetic helicity flux into the solar atmosphere can be separated on two components, one due to vertical advection of twisted magnetic field through the photosphere and one due to "braiding" of fields by the differential rotation or other large-scale horizontal motions. The contribution of differential rotation to the helicity budget was quantified for active regions (DeVore 2000) and for the large-scale solar magnetic field (Berger & Ruzmaikin 2000). The braiding contribution was observationally measured (Chae 2001; Moon et al. 2002) and found to greatly exceed the contribution which might have been provided by differential rotation alone. This higher level of helicity transport is also required to account for the helicity loss by coronal mass ejections which has been found to greatly exceed the production possible by differential rotation (Démoulin et al. 2002; Green et al. 2002).

Helicity flux studies therefore imply that magnetic helicity transport into active region magnetic fields results, at least in part, from local photospheric flow fields. Since the active region magnetic helicity exhibits a correlation with latitude (Pevtsov et al. 1995), these local flows must be arranged to inject (preferentially) negative helicity into Northern regions and positive helicity into Southern fields. It is common to assume that photospheric flows will be affected very little by the magnetic field itself since the *average* plasma β is small. This means

that local photospheric flows of non-magnetic origin are responsible for injecting helicity into the active region corona.

Longcope & Welsch (2000) reasoned, however, that vortical motions responsible for helicity injection cannot be driven by pressure gradients, and cannot easily by produced by coupling motions of non-magnetic plasma to the active region itself. Moreover, any magnetic torques arising from the active region's sub-photospheric field cannot be countered by pressure gradients. They demonstrated this in a model wherein a twisted sub-photospheric flux tube drove photospheric flows to transport helicity into the active region above it. These flows were components of torsional Alfvén wave which transported helicity along the length of the flux tube. The model made the further prediction that an emerging active region would develop twist on a time scale of roughly one day: the Alfvén travel time over the sub-photospheric axis containing the helicity required by the coronal field.

The time evolution of coronal twist during the emergence of an active region can be used to infer the mechanism driving the photospheric flows which transport magnetic helicity. Flows of non-magnetic origin would drive passive magnetic fields, injecting helicity at a rate unrelated to the active region's emergence. There is no reason to expect these flows to be coordinated with emergence, so almost any time-history would be possible. On the other hand, if the flows are driven by magnetic torques the coronal twist would evolve similarly in every emerging region: beginning small or zero initially and ramping up to a final value. The time scale of the ramp-up would be the longer of the sub-photospheric Alfvén time and the polarity separation time (Longcope & Welsch 2000).

Based on observations of coronal twist evolution during the emergence of six different active regions we conclude that helicity is injected by magnetically driven flows. We find that each active region's twist exhibits the characteristic evolution described above, and can even be fit to a quantitative model of twist evolution. In the next section we describe our data and how it is used to measure coronal twist and other aspects of flux tube emergence. Section 3 presents the results of these observations and describes the generic active region development and coronal twist evolution. Section 4 presents a model for the coupling of helicity from a twisted flux tube to an emerging active region. This model is then fit numerically to the observed twist evolutions. This fitting yields an estimate of the sub-photospheric flux tube's Alfvén velocity at a depth of 5–10 Mm. The subsequent section examines the implications of these results on theories of generation and transport of magnetic helicity.

2. Data

Our ultimate objective is to quantify the magnetic helicity in the coronal fields of active regions as they emerge. To actually calculate the (relative) helicity would require a three-dimensional grid of vector field measurements throughout the corona; a measurement of this kind has never been made. The alternative is either to calculate the helicity of a model coronal field (Démoulin et al. 2002) or to integrate the photospheric helicity flux, which is found from surface maps of all three components of the magnetic field and the plasma velocity (Kusano et al. 2002). High time-cadence vector magnetic field measurements of emerging active regions are extremely rare (a point to which we return below), so we are forced to estimate the magnetic helicity from a model magnetic field constructed using only line-of-sight field measurements.

The magnetic field measurements we use for this purpose are full-disk, line-of-sight magnetograms from the Michelson Doppler Imager (MDI, Scherrer et al. 1995) on board of the Solar and Heliospheric Observatory (SoHO, Domingo, Fleck, & Poland 1995). These magnetograms have spatial resolution of 1.98 arc sec per pixel and are available at a time cadence of 96 minutes for virtually the entire period since SoHO was launched. The simplest magnetic model which can be constructed from these measurements is a linear force-free field (LFFF) satisfying $\nabla \times \mathbf{B} = \alpha \mathbf{B}$, where α is the single free parameter of the model. Unfortunately, not even this simple model can be constrained using line-of-sight magnetograms alone, so we must introduce at least one piece of additional data.

We constrain the parameter α by comparing field lines from the model to EUV images of the active region. For this comparison we use 195Å images (Fe XII) full-disk images from Extreme ultraviolet Imaging Telescope (EIT, Delaboudiniere, et al. 1995) on board SoHO, which have a resolution of 2.63 arc sec per pixel. We require that the MDI and EIT observations be within a few minutes to obviate the need to correct for solar rotation when comparing the two data sets. The LFFF matching the line-of-sight field is found for a specified value of α, and then numerous field lines are plotted over the co-aligned EIT image. This procedure is repeated for a range of α values and that value is selected whose model field lines most resembled the bright coronal structures of the EIT image.

This fitting method yields a parameter α which characterizes twist in the coronal magnetic field of the active region as a whole. The method seems subjective since an observer must decide when field lines best fit bright EUV structures. Furthermore, the method tacitly assumes that the active region field has a single sense of twist and that structures visible in EIT 195 Å images actually follow magnetic field lines. There is evidence, however, in a study by Burnett et al. (2003), that the value of α so found is a good proxy for more accurate measures of overall magnetic twist. Burnette et al. calculated magnetic twist in two inde-

pendent ways for each of 34 mature active regions observed with both vector magnetograms and Yohkoh Soft X-ray images. One measure of twist, which they call α_c and is identical to our α, was found by fitting a LFFF to the vertical field and adjusting α to best match bright features in the coronal image. An independent twist parameter was provided by $\alpha_{\rm best}$ which involves all three of the measured photospheric field components. This measure of twist, introduced by Pevtsov et al. (1995), has been used extensively to characterize the twist in active magnetic fields (Pevtsov et al. 1997; Longcope et al. 1999; Longcope & Pevtsov 2003). Burnette et al. found that the two different measures of average twist were highly correlated (Spearman $\rho = 0.71$) and fit a line $\alpha_c = (0.91 \pm 0.13)\alpha_{\rm best}$. We therefore conclude that α_c may be used as a proxy for $\alpha_{\rm best}$ in those cases where vector magnetograms are unavailable.

We began by selecting a set of emerging active regions on which to perform our study. Using Solar-Geophysical Data (SGD) monthly reports we identified several regions that emerged East of central meridian. Next we used MDI and EIT records to select those emerging regions that were well observed by both instruments. Table 1 lists the six active regions satisfying this criterion which we use in our study.

The coronal fitting method was then applied to each each pair of MDI/EIT images to yield a value of α at that time. The active region was further characterized by the flux in each polarity and the separation d between poles. On each magnetogram we visually located points approximating the positions of the negative and positive polarities. The contiguous region above a fixed threshold (50 G) which included the "pole point" was defined as the polarity region. The total flux in this region was the pole's flux, and its center of figure (weighted by the unsigned magnetic flux) was its location. The image coordinates of the polarity centers were converted into heliospheric coordinates and the separation calculated in heliographic degrees; this distance was then converted to megameters. In all cases the magnetic flux and its area grew steadily as the active region emerges and evolves.

Uncertainties in α were estimated by using the late, stable period (when the coronal images did not change significantly) in each active region's evolution. Assuming the coronal field was in fact static during this period, each measurement of α is an independent measurement of the same quantity, and the standard deviation, $\sigma\alpha$, is an estimate of the measurement error. We apply this estimate of uncertainties to α throughout the emergence of that particular active region. Uncertainties in total flux and footpoint separation are extremely small since each value arises from the sum over a hundred or more pixels.

3. Evolution of Active Regions and Their Twist

Figure 1 shows the early evolution of emerging region NOAA AR 9139. The magnetic field associated with the region can be first identified around 19 August, 12:47 UT (Figure 1a) and within a day it develops into a distinct bipolar region. Figure 2 shows the evolution of magnetic parameters of this region, i.e., twist α, polarity separation d, magnetic flux and total area. Polarity separation and magnetic flux are corrected for projection. As the active region develops both its total area and magnetic flux grow. The polarity separation increases and reaches a plateau ≈ 1.5 days after the beginning of emergence. On the other hand the α-coefficient increases much faster and it reaches the plateau in less than a day. This behavior is reminiscent of "slow emergence" scenario in Longcope & Welsch (2000). Figure 3 gives an example of another emerging region NOAA AR 8817. As with NOAA AR 9139 the evolution of this region corresponds to "slow emergence" scenario, although the evolution of α is much noisier as compared with Figure 2.

Not all active regions exhibit monotonic increase in α and polarity separation as Figure 2, e.g. in case of NOAA AR 8768 (Figure 4) both polarity separation and α decreased after an initial period of growth. However, upon close examination of magnetograms of this region we found that another region was emerging in close proximity. Thus, we believe that our method of fitting overall coronal structure to a photospheric magnetogram may be affected by this new flux emergence.

4. A Model of Emergence

A model of an emerging twisted flux tube was developed by Longcope & Welsch (2000). They began by assuming the evolution to be slow enough that the coronal field remains in force-free equilibrium characterized by its total relative helicity H_R. For a constant-α field with footpoint separation d, the relative helicity within the active region is approximately

$$H_R \simeq \frac{\Phi^2}{2\pi}\alpha d \quad , \tag{1}$$

where Φ is the net magnetic flux in either pole. If no helicity were added then the magnitude of α would decrease as d increased; in fact α is observed to increase along with d.

Relative helicity will be added to or removed from the corona by motion of the photospheric polarities. Approximating the polarities as small, unipolar patches the change in relative helicity is (Berger & Field 1984; Longcope & Pevtsov 2003),

$$\frac{dH_R}{dt} = -\frac{\Phi^2}{2\pi}(\omega_+ + \omega_-) \quad . \tag{2}$$

where ω_+ and ω_- are the angular velocities with which the positive and negative polarities spin about the vertical.

Each photospheric polarity is the terminus of a flux tube extending into the convection zone. A spinning motion of this terminus must arise from a torque exerted either by the flux tube beneath or by the photospheric plasma surrounding it. We will neglect the latter possibility due to numerous uncertainties in the process of coupling the magnetic and non-magnetic components at high Reynolds number (Longcope & Pevtsov 2003). We therefore consider only effects internal to the flux tube. The dynamics of a twisted flux tube have been modeled under the approximation that its cross section is sufficiently thin (Longcope & Klapper 1997).

We will henceforth adopt this thin flux tube approximation and parameterize each axis by a length coordinate s increasing toward the photosphere at $s = 0$. The field lines twist about the axis at a local pitch $q(s)$, such that a given field line would wrap once over a length $\Delta s = 2\pi/|q|$ in a right handed helix for $q > 0$ and left handed helix for $q < 0$. The material in the tube spins about the axis at angular velocity $\omega\hat{\mathbf{s}}$, where $\hat{\mathbf{s}}$ is the axial tangent vector. Neglecting motion of the axis itself, the twist and spin satisfy the telegrapher's equations (Longcope & Klapper 1997; Longcope & Pevtsov 2003)

$$\frac{\partial q}{\partial t} = \frac{\partial \omega}{\partial s} \quad , \tag{3}$$

$$\frac{\partial \omega}{\partial t} = v_{\rm A}^2 \frac{\partial q}{\partial s} \quad . \tag{4}$$

where $v_{\rm A}$ is the Alfvén speed along the tube's axis.

Under the further assumption of uniform Alfvén speed Eqs. (3) and (4) admit solutions in the form of arbitrary incident and reflected wave forms $w_i(t)$ and $w_r(t)$,

$$q(s,t) = w_r(t + s/v_{\rm A}) + w_i(t - s/v_{\rm A}) \quad , \tag{5}$$

$$\omega(s,t) = v_{\rm A}\,[\,w_r(t + s/v_{\rm A}) - w_i(t - s/v_{\rm A})] \quad . \tag{6}$$

A flux tube in uniformly twisted equilibrium requires a continual reflection off of the photospheric boundary so that $w_r = w_i = q/2$.

The twisted flux tube carries an internal, axial current $I = 2q\Phi$ along its field lines and an opposing return current at its surface. To maintain force balance across the photosphere the interior current must pass into the corona so $\alpha = 2q$ (Longcope & Welsch 2000). This condition at $s = 0$ is what determines the reflection of torsional waves off the photospheric surface: $w_r(t) = \alpha(t)/2 - w_i(t)$. According to Eq. (6) the observed photospheric motion is a combination of the incident and reflected waves. Using the expression for the reflection

yields the photospheric angular velocities

$$\omega_{\pm} \;=\; \tfrac{1}{2} v_{\rm A} \alpha \;-\; 2 v_{\rm A} w_{i,\pm} \quad , \tag{7}$$

where $w_{i,+}$ and $w_{i,-}$ are the wave forms incident on the positive and negative poles respectively. Thus the photospheric sources will spin if the twist incident from depth is not properly matched to the coronal twist, α.

Using the boundary condition (7) in the helicity evolution, (2), yields an expression for the evolution of α

$$2\pi\Phi^{-2}\frac{dH_R}{dt} = d\dot{\alpha} \;+\; \alpha\dot{d} = -v_{\rm A}\left(\alpha - 2w_{i,+} - 2w_{i,-}\right) \quad . \tag{8}$$

If both polarities are anchored to flux tubes which were initially uniformly twisted with $q = \bar{q}$, then the incident waves from each side will be $w_{i,\pm} = \bar{q}/2$. Under this assumption the coronal twist will evolve according to

$$\frac{d\alpha}{dt} + \frac{\dot{d}}{d}\,\alpha \;=\; -\frac{v_{\rm A}}{d}\left(\alpha - \bar{\alpha}\right) \quad , \tag{9}$$

where $\bar{\alpha} \equiv 2\bar{q}$ is the asymptotic value for the coronal twist α.

4.1. Fitting the data

In general the observed active regions begin with no measurable twist at the instant of emergence t_0, so we will take $\alpha(t_0) = 0$. Observations strongly suggest that the emergence process can be modeled as a linear increase in separation beginning with $d(t_0) = d_0$. The separation increases at constant rate $\dot{d}$ until a time t_1, after which d remains constant,

$$d(t) \;=\; \begin{cases} d_0 + \dot{d}(t - t_0) & , \quad t_0 \le t \le t_1 \\ d_0 + \dot{d}(t_1 - t_0) \equiv d_1 & , \quad t_1 < t \end{cases} \tag{10}$$

The solution to (9) for the emergence period, $t_0 \le t \le t_1$ is

$$\alpha = \bar{\alpha}\,\frac{\nu}{\nu+1}\left[1 - \left(\frac{d}{d_0}\right)^{-(\nu+1)}\right] \tag{11}$$

where $\nu \equiv v_{\rm A}/\dot{d}$. This form for $\alpha(t)$ differs from that derived by Longcope & Welsch (2000), who assumed a different form for $d(t)$.

During the post-emergence period, where $\dot{d} = 0$ and $d = d_1$, α approaches $\bar{\alpha}$ exponentially with time constant, $d_1/v_{\rm A}$. The explicit form of observed coronal twist for both periods is

$$\alpha(t) = \begin{cases} \bar{\alpha}\,\dfrac{\nu}{\nu+1}\left\{1 - \left[1 + \dfrac{\dot{d}}{d_0}(t-t_0)\right]^{-(\nu+1)}\right\} & , \quad t_0 \le t \le t_1 \\ \\ \bar{\alpha} + (\alpha_1 - \bar{\alpha})\,\exp\left[\dfrac{-v_{\rm A}(t-t_1)}{d_1}\right] & , \quad t_1 < t \end{cases} \tag{12}$$

where $\alpha_1 = \alpha(t_1)$.

The data described in Section 3 (except for AR 8738 for which $\alpha \simeq 0$) are fit to the above model in a two step procedure. First the separation curve is fit to model (10). The beginning and ending times for emergence, t_0 and t_1 are identified by inspection. Then d_0 and $\dot{d}$ are determined by fitting the measured values of d to a linear function of t (over the interval $t_0 \le t \le t_1$) using linear least-squares. With these values fixed, ν and $\bar{\alpha}$ are the only free parameters remaining in expression (12). Measured values of α from times $t < t_1$ are fit to that functional form using non-linear least squares. Figure 5 shows typical fits, AR 9139 and AR 8587, along with the somewhat problematic case of AR 9193. The parameters found from fitting all data sets are listed in Table 2.

The instrumental uncertainties in the separation d are expected to be extremely small, as discussed in section 2. We therefore use the linear fit itself to estimate the uncertainties in the parameter $\dot{d}$ (Bevington & Robinson 1992). These turn out to be extremely small, owing to the remarkably linear behavior in $d(t)$. As described in section 2, uncertainties in the twist parameter α are estimated by assuming the final phase in its time evolution is a constant value plus measurement errors. These uncertainties are used to estimate uncertainties in fitting parameters, ν and $\bar{\alpha}$ by Monte Carlo technique: one thousand synthetic data sets, measurements plus additional random noise, are constructed and then fit (Press et al. 1986). These uncertainty estimates are larger and more realistic than the classical estimates defined by $\Delta\chi^2 \le 1$. The uncertainty in $v_{\rm A}$ are found by adding in quadrature the relative errors in $\dot{d}$ and ν.

The model fits all of the data sets well, as typified by Fig. 5. Values of χ^2_ν are all above unity, as expected for an imperfect model of reality. It might also be the case that our estimates of $\sigma\alpha$ are systematically small since they are made during the late quiescent phase of evolution. For example, Figure 3 shows much more point-to-point scatter in the early phase than the later phase from which $\sigma\alpha$ was found. This may be an important factor in the large value of χ^2_ν for NOAA AR 8817.

From expression (11) it can be seen that α_1 is smaller than $\bar{\alpha}$ at least by a factor $\nu/(\nu+1)$. It is therefore not surprising that the parameter $\bar{\alpha}$ found from each fit exceeds, by at least a factor of two, the largest measured values of α. According to the post-emergence curve, $\alpha(t)$ should approach $\bar{\alpha}$ on a time-scale $d_1/v_{\rm A}$, typically about five days in these cases. Thus we observe very little change in α over the one to two days observed after the active region has completely emerged.

The greatest discrepancy between $\bar{\alpha}$ and α_1, a factor of eight, was found in AR 9193 (bottom of Fig. 5). This active region was notable for its complex twist-history which included a half-day latency following emergence and a decrease while $\dot{d}$ was still positive. We consider the implications of this complex evolution in the next section.

The case of AR 8738, $\alpha(t) \simeq 0$, can be fit trivially by taking $\bar{\alpha} = 0$. This reflects the fact that if an untwisted flux tube emerges the coronal field will remain potential. This degenerate case provides no information about ν or $v_{\rm A}$.

The ratio $\nu = v_{\rm A}/\dot{d}$ is considered a free parameter in our fitting. This means that we are using coronal observations to "measure" the sub-photospheric Alfvén speed. This is a reasonable approach considering that there are no direct means of observing the magnetic field at depths of 5–10 Mm. Furthermore, our model assumes the sub-photospheric Alfvén speed to be constant, for simplicity. The value of $v_{\rm A}$ found by our fitting should thus be interpreted as an *average* sub-photospheric Alfvén speed. It is rather encouraging that all five cases considered yield similar Alfvén speeds, roughly 100 m/sec. We consider below the reasonableness of this value for flux tubes beneath active regions.

5. Discussion

The foregoing analysis quantified the overall twist in the coronal field by the extrapolating a linear force-free field from photospheric magnetograms and adjusting α by comparisons of field lines to coronal images. While a more straightforward and accurate measurement of α is possible using vector magnetograph (VMG) data (Pevtsov et al. 1995), this is not practical for the present study. One difficulty with its application is that all vector magnetographs are presently on ground-based telescopes and therefore cannot provide continuous multi-day observations. Another difficulty is that vector magnetograms of the very early stages of emerging active regions are almost non-existent.

One particular observation does exist with which we might check our findings. Figure 6 shows very rare observations (by Haleakala Stokes Polarimeter, Mickey 1985) of emerging region close to a pre-existing leading polarity sunspot. We used the vector magnetograms

to derive a different measurement of overall twist, $\alpha_{\rm best}$ following Pevtsov et al. (1995). Computing it separately for existing flux (filled circles) and emerging fluxes (open circles) shows an evolution of $\alpha_{\rm best}$ for the emerging flux (Figure 6) similar to that exhibited by coronal-fit α in regions from our study, e.g. Figures 2 and 3. The twist $\alpha_{\rm best}$ in the emerging features (open circles) increases in magnitude (it is negative) from Aug. 17 until it peaks on Aug. 19. This coincides with the separation of the polarities (squares). Thus we find that a more accurate estimate of twist shows the same pattern of evolution as do our coronal-fit measurements. This conforms to the expectation born of the work by Burnette et al. (2003) which established that α could be used as a proxy for $\alpha_{\rm best}$.

Using the coronal-fitting technique we compiled data for six different emergences. These showed a general trend for the coronal twist to increase at roughly the same time as the polarities separated. It is notable that the twist can reach a plateau either before or after the separation does. In four cases α plateaus earlier than the polarity separation, while in one case (NOAA AR 8582) α plateaus later. (In the sixth case, NOAA AR 8738, we find no change in α even as the active region grows). This range of behavior is not easily reconciled with simple scenarios of helicity injection, but *is* predicted by the twist injection model (Longcope & Welsch 2000).

In all cases studied the magnetic field appears to be untwisted at the beginning of emergence; in all cases but one (AR9193) α increases during emergence and reaches a plateau within $\sim$ 0.8-1.7 days. The active region has therefore gained helicity during the process of emergence. We can estimate the final helicity of each active region from Eq. (1), using α and d values already found and defining Φ as half the unsigned flux of the AR.[2] The resulting helicities, listed in Table 3, are typically 10^{41} Mx^2, comparable to AR helicities found by other means (Green et al. 2002).

The helicity flux through the photospheric surface ($z = 0$) is

$$\frac{dH_R}{dt} \;=\; 2\int (\mathbf{A}_p \cdot \mathbf{B}_\perp) v_z \, dx\, dy \;-\; 2\int (\mathbf{A}_p \cdot \mathbf{v}_\perp) B_z \, dx\, dy \quad , \tag{13}$$

where $\mathbf{A}_p$ is the vector potential of a potential field matching the vertical photospheric field B_z (Berger & Field 1984). The first and second terms on the right hand side of this expression are contributions due to vertical motions v_z (emergence) and due to horizontal motions $\mathbf{v}_z$ (braiding). Vertical motions transport helicity by advecting twisted field across the photospheric surface. If this mechanism were dominant we would expect the twist of the coronal field to remain at a constant value, $\alpha \sim \bar{\alpha}$, throughout the emergence process. In

[2]The magnetic flux was corrected by a factor of 0.64 following Berger & Lites (2003), who showed that the MDI calibration underestimates the true flux densities by a factor of 0.64 (plage) and 0.69 (sunspots).

this scenario H_R increases in proportion to Φ^2 as pre-twisted flux is moved into the corona. Our data shows, to the contrary, that α begins small and increases at the same time Φ is increasing. Thus we conclude that helicity is transported into the corona primarily by horizontal photospheric motions.

The horizontal photospheric motions responsible for helicity transport can have two basic causes. They may be flows of the unmagnetized plasma which affect an apparently passive magnetic flux, or they may be flows driven by magnetic forces. It is often assumed that magnetic forces will not be effective in the photosphere and convection zone where β is typically large. Therefore active region fields are often modeled as if their lower boundary were "driven" by prevailing motions such as differential rotation.

DeVore (2000) applied the passive-advection approach to calculate the helicity flux into a bipolar active region whose photospheric footpoints moved according to differential rotation. The resulting helicity flux depended on the latitude, separation and *tilt angle* of the bipole. If all of these factors were optimally chosen the helicity flux could be as large as $dH_R/dt \simeq 3 \times 10^{-3}\Phi^2/$ day. When applied to our sample, this value is smaller, typically by an order of magnitude, than the helicity flux we actually observe. Thus we can reject differential rotation as a possible source of helicity injection.

The ineffectiveness of differential rotation does not mean that photospheric motions cannot inject significant helicity. Chae (2001) and Nindos & Zhang (2002) both used local correlation tracking techniques to measure horizontal motions and thereby compute helicity fluxes. The helicity injection rates they computed were significantly larger than differential rotation could supply. Indeed, the flow patterns found by the tracking technique are highly localized and appear unrelated to differential rotation. These observations cannot, however, shed light on whether the observed motions are driven by magnetic or non-magnetic forces.

The clear relationship between $\alpha(t)$ and $d(t)$ in all cases observed strongly suggests that helicity is injected by flows driven by the emergence itself. Had the field instead evolved under the influence of existing local flows there would be no reason to expect the helicity injection to be related to the emergence as we observe it to be. Thus we propose that magnetic forces within the emerging active region drive the flows which transport helicity into the corona.

We propose a model of these magnetically driven flows and find that it fits every one of our observed emergences. In this model the twist from the flux tube propagates as torsional Alfvén waves, ultimately supplying the coronal field with helicity. The natural time-scale for this process is governed by the Alfvén speed within the tube and the rate of polarity separation. We fit the observations by tuning the Alfvén speed, as shown in Table 2. Since

the ramp-up time for α is typically one day, the torsional Alfvén waves will have propagated from that depth. This is a depth of ~ 8 Mm, using the inferred speed of $v_{\rm A} \sim 100\,{\rm m/sec}$. At this depth $\rho \simeq 4 \times 10^{-4}$, and a flux tube of $B = 10^3$ G has an Alfvén velocity 140 m/sec, consistent with our results.

It is worth noting that our model of flux tube *emergence* omits helicity transport by the "emergence term". The reason for omitting the term is that so little mass can enter the corona, where the density is 10^{-9} times smaller than in the convection zone. Instead the tube's twist drives rotational photospheric flow which supplies helicity through the "braiding term" of eq. (13).

The model makes numerous simplifying assumptions which are intended to be a crude approximation of reality. We characterize the active region field by a single twist α and use a simple estimate of the relative helicity, (1), which ignores all of the region's geometry except its polarity separation. Furthermore, we assume the sub-photospheric flux tube is thin and has a uniform Alfvén speed. In light of these approximations we expect the parameters found by our fitting to be only rough estimates of e.g. the sub-photospheric Alfvén speed.

We also made the assumption that the emerging flux tube had been uniformly twisted, $q = \bar{\alpha}/2$, prior to emergence. This assumption allowed us to use simple incident wave-forms, $w_{i,\pm} = \bar{\alpha}/4$ in our model of $\alpha(t)$. Had the tube contained some complex pattern of twist, $q(s)$, the incident wave-forms would be similarly complex. We suggest that the complex time-history of α observed in AR9193 is evidence of such a complex twist pattern. The time history consists of a period of latency ($0.5 < t < 1.1$ days) followed by rapid increase ($1.1 < t < 2.1$), and then a decrease. This pattern would occur under the incidence of a wave-form which was low, then high, then negative. Such variable twist patterns would occur quite naturally if the twist were introduced by turbulent distortion of the tube's axis as by the Σ-effect (Longcope et al. 1998).

6. Conclusion

By studying the twisted coronal field during the course of emergence we have found evidence for the sub-photospheric origin of magnetic helicity. We quantify the coronal twist in terms of an α-parameter. This is measured by comparing observed coronal structures to extrapolated field lines. Each of the five active regions emergences show α beginning at zero and increasing to a plateau within 1.5 days. We fit these time histories to a model of the emergence of a twisted sub-photospheric flux tube. The implication of this fitting is that helicity is generated in the solar interior and transported into the corona through

the emergence of twisted flux tubes. The helicity transport across the photosphere occurs primarily due to spinning of the active region polarities driven by magnetic torque from below.

D. W. L. has been supported by NASA through grant NAG 5-6110. SoHO is a project of international cooperation between ESA and NASA. Data used here from Mees Solar Observatory, University of Hawaii, are produced with the support of NASA grant NAG 5-4941 and NASA contract NAS8-40801. We thank the anonymous referee for helpful comments on the manuscript.

REFERENCES

Bao, S,. & Zhang, H. 1998, ApJ, 496, L43

Berger, M. A., & Field, G. B. 1984, J. Fluid Mechanics, 147, 133

Berger, M. A., & Ruzmaikin, A. 2000, J. Geophys. Res., 105, 10481

Berger, T., & Lites, B. W. 2003, Sol. Phys., in press

Bevington, P. R. & Robinson, D. K., 1992, *Data Reduction and Error Analysis for the Physical Sciences*, Second Edition, McGraw-Hill, Boston, MA

Burnette, A. B., Canfield, R. C., & Pevtsov, A. A. 2003, ApJ, submitted

Chae, J. 2001, ApJ, 560, L95

Delaboudiniere, J.-P., et al. 1995, Sol. Phys., 162, 291

Démoulin, P., Mandrini, C. H., van Driel-Gesztelyi, L., Thompson, B., Plunkett, S., Kővári, Z., Aulanier, G., & Young, A. 2002, A&A, 382, 650

DeVore, C. R. 2000, ApJ, 539, 944

Domingo, V., Fleck, B., & Poland, A. I. 1995, Sol. Phys., 162, 1

Emonet, T., & Moreno-Insertis, F. 1998, ApJ, 492, 804

Fan, Y., Zweibel, E. G., & Lantz, S. R. 1998, ApJ, 493, 480

Green, L. M., López Fuentes, M. C., Mandrini, C. H., Démoulin, P., Van Driel-Gesztelyi, L., & Culhane, J. L. 2002, Sol. Phys., 208, 43

Grigoryev, V. M., & Ermakova, L. V. 2002, Sol. Phys., 207, 309

Kusano, K., Maeshiro, T., Yokoyama, T. & Sakurai, T., 2002, ApJ577, 501

Leka, K. D., Canfield, R. C., McClymont, A. N., & Van Driel-Gesztelyi, L. 1996, ApJ, 462, 547

Longcope, D. W., Fisher, G. H., & Pevtsov, A. A. 1998, ApJ, 507, 417

Longcope, D. W., & Klapper, I. 1997, ApJ, 488, 443

Longcope, D. W., Linton, M. G., Pevtsov, A. A., Fisher, G. H., & Klapper, I. 1999, in Magnetic Helicity in Space and Laboratory Plasmas, ed. M. R. Brown, R. C. Canfield, & A. A. Pevtsov (Washington, D.C.: AGU), 93

Longcope, D. W., & Pevtsov, A. A. 2003, Advances in Space Research, in press

Longcope, D. W., & Welsch, B. T. 2000, ApJ, 545, 1089

Mickey, D. L. 1985, Sol. Phys., 97, 223

Moon, Y.-J., Chae, J., Choe, G. S., Wang, H., Park, Y. D., Yun, H. S., Yurchyshyn, V., & Goode, P. R. 2002, ApJ, 574, 1066

Nindos, A., & Zhang, H. 2002, ApJ, 573, L133

Pevtsov, A. A., Canfield, R. C., & McClymont, A. N. 1997, ApJ, 481, 973

Pevtsov, A. A., Canfield, R. C., & Metcalf, T. R. 1995, ApJ, 440, L109

Press, W. H., Flannery, B. P., Teukolsky, S. A., & Vetterling, W. T., 1986, *Numerical Recipes: The Art of Scientific Computing*, Cambridge University Press, Cambridge, UK

Portier-Fozzani, F., Aschwanden, M., Démoulin, P., Neupert, W., Delaboudinière, J.-P., & the EIT Team 2001, Sol. Phys., 203, 289

Scherrer, P. H., et al. 1995, Sol. Phys., 162, 129

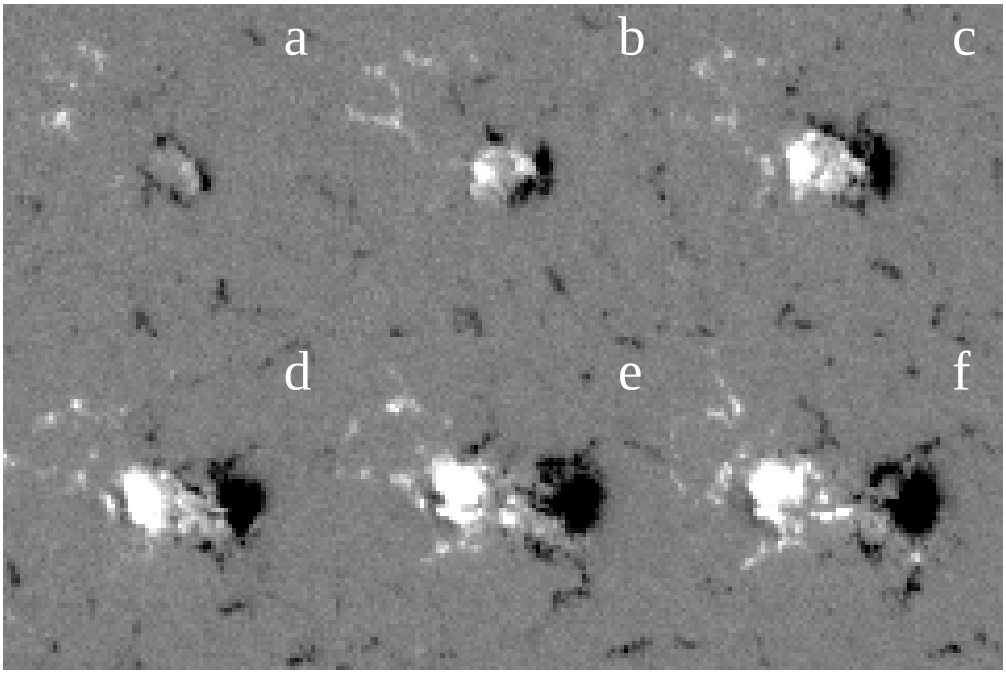

Fig. 1.— Emergence of active region NOAA AR 9139. (a) – 19 Aug. 2000, 1247 UT, (b) – 19 Aug. 2000, 2047 UT, (c) – 20 Aug. 2000, 0447 UT, (d) – 20 Aug. 2000, 1247 UT, (e) – 20 Aug. 2000, 2047 UT, (f) – 21 Aug. 2000, 0447 UT. White (black) indicates positive (negative) polarity.

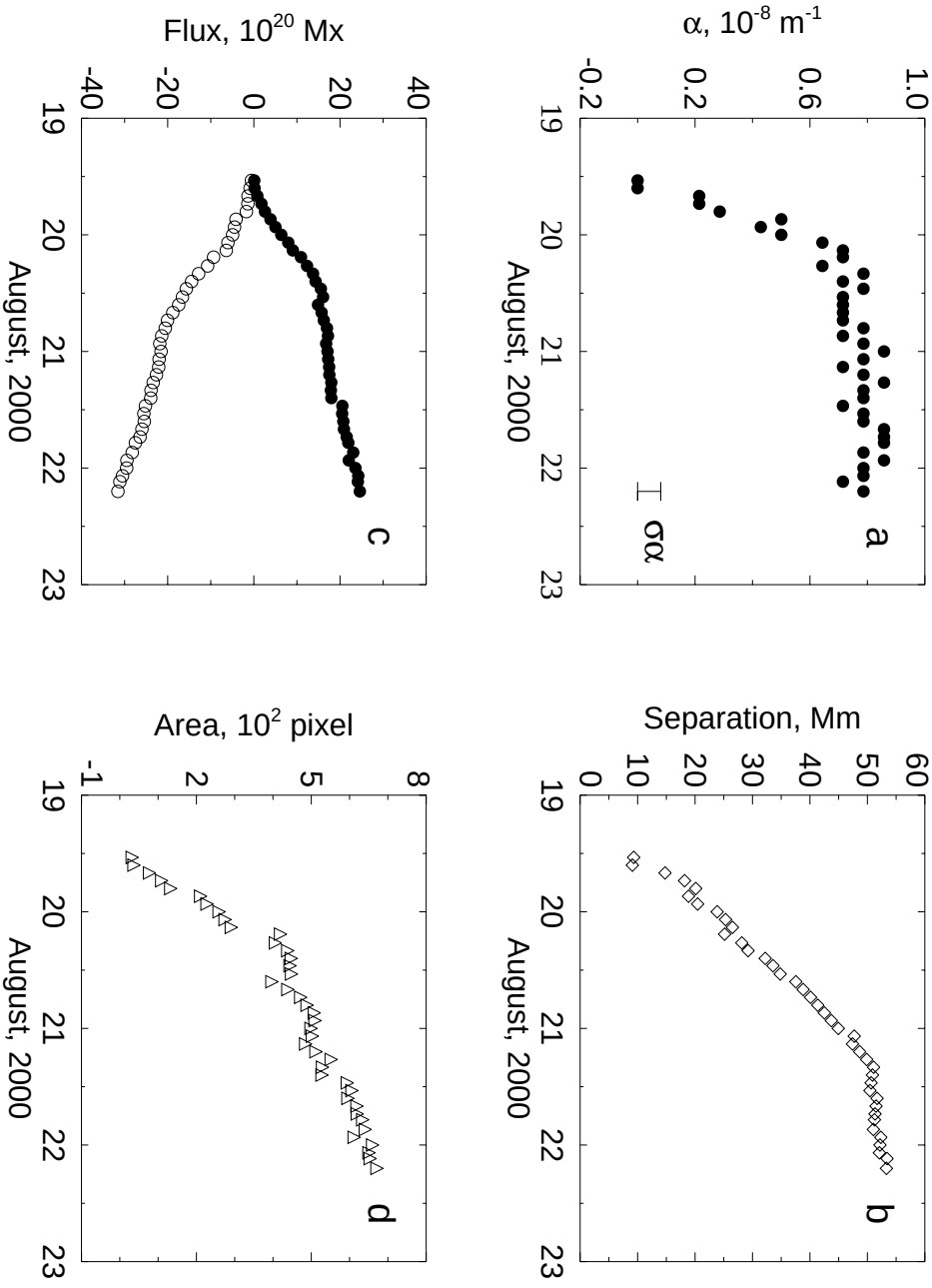

Fig. 2.— Evolution of magnetic parameters of NOAA AR 9139. (a) – α, (b) – polarity separation, (c) – magnetic flux and (d) – total area.

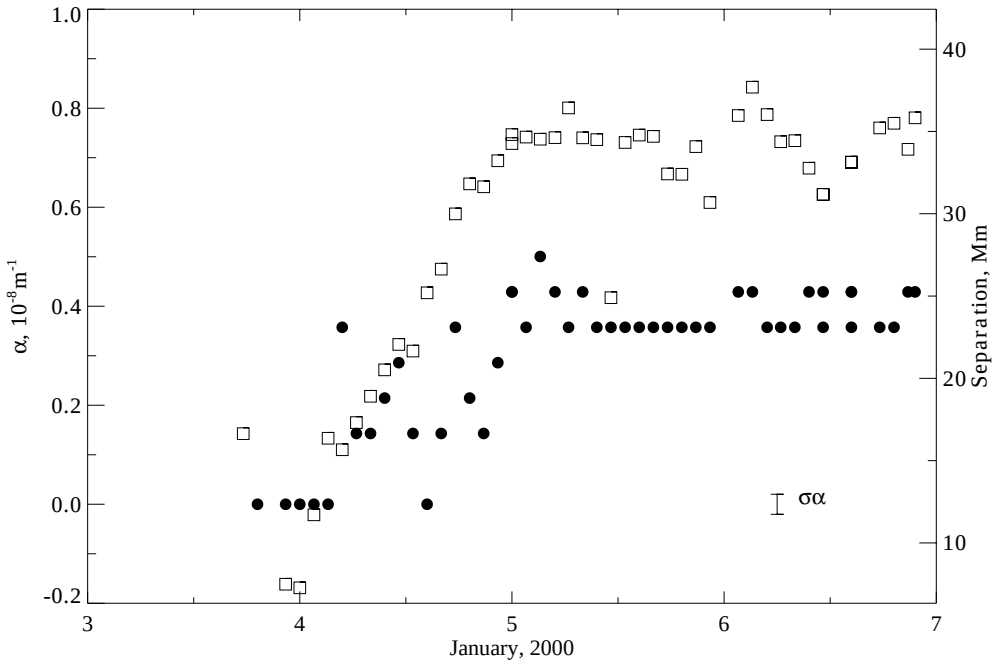

Fig. 3.— Active region NOAA AR 8817, filled circles show α and squares are polarity separation.

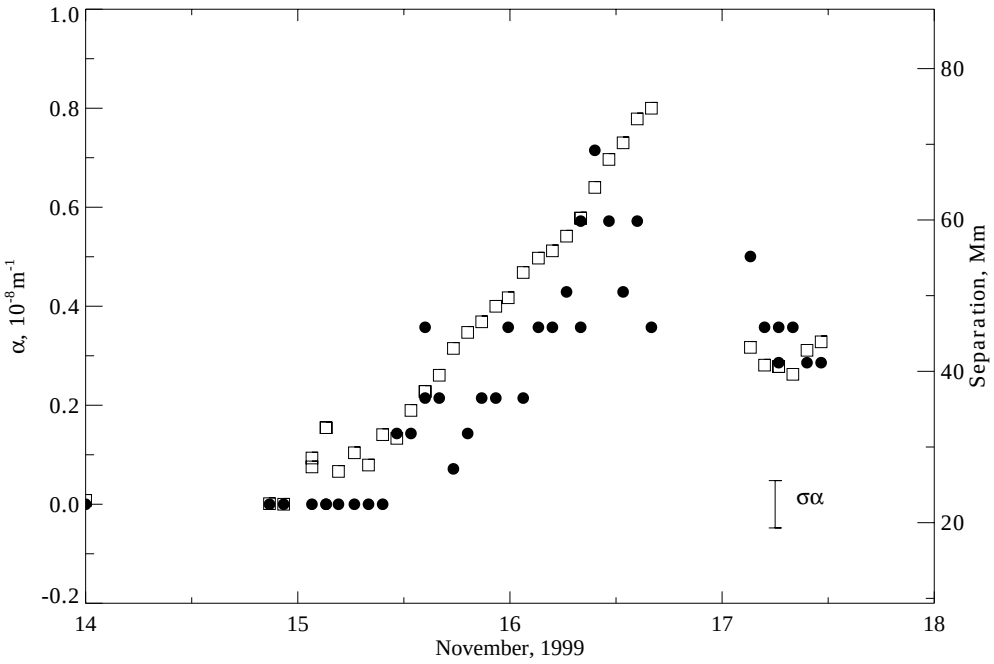

Fig. 4.— Active region NOAA AR 8768, filled circles show α and squares are polarity separation.

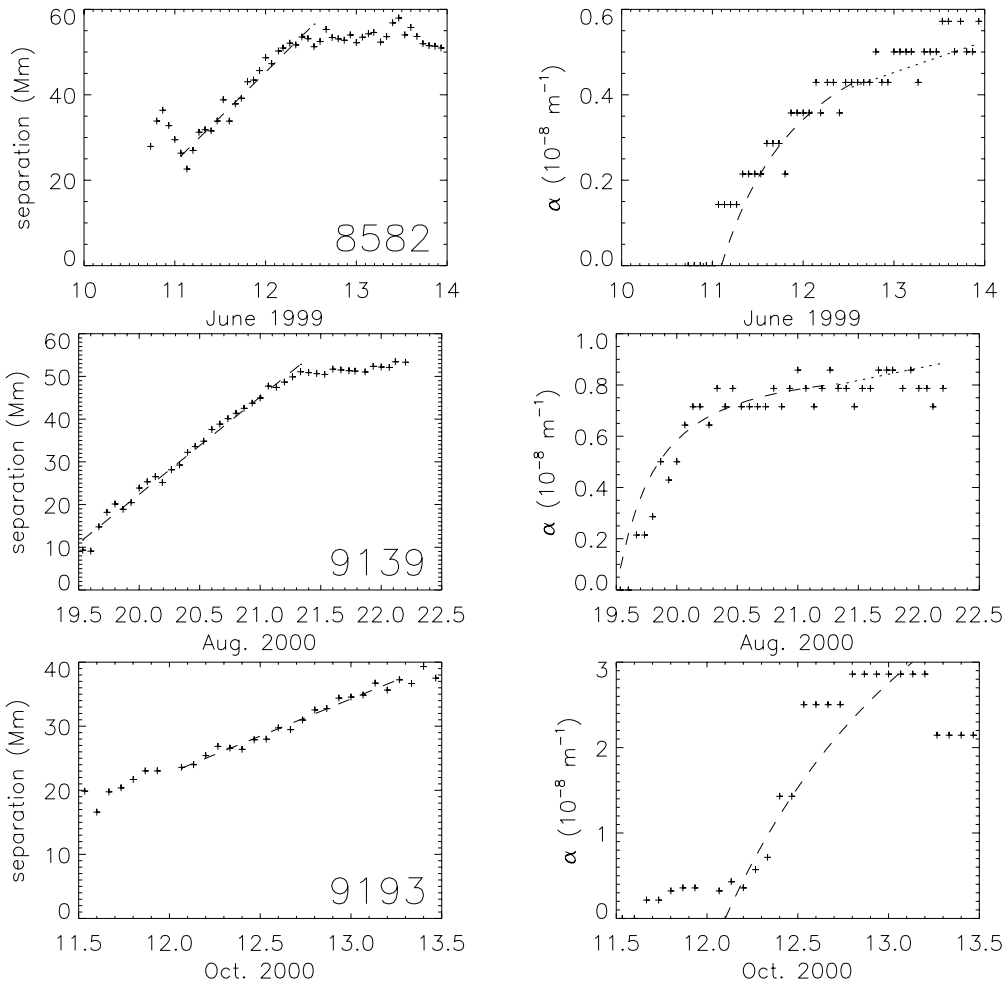

Fig. 5.— Active regions NOAA 8582 (top row), NOAA 9139 (middle row), and NOAA 9193 (bottom row) fit to the emergence model. The left panels show measured separation d (pluses) and the fit (dashed) out to t_1. The Right panels show measured twist α (pluses) and the fit (dashed) done for $t_0 \leq t \leq t_1$. The dotted line shows the model for evolution after t_1, for which there are no remaining free parameters.

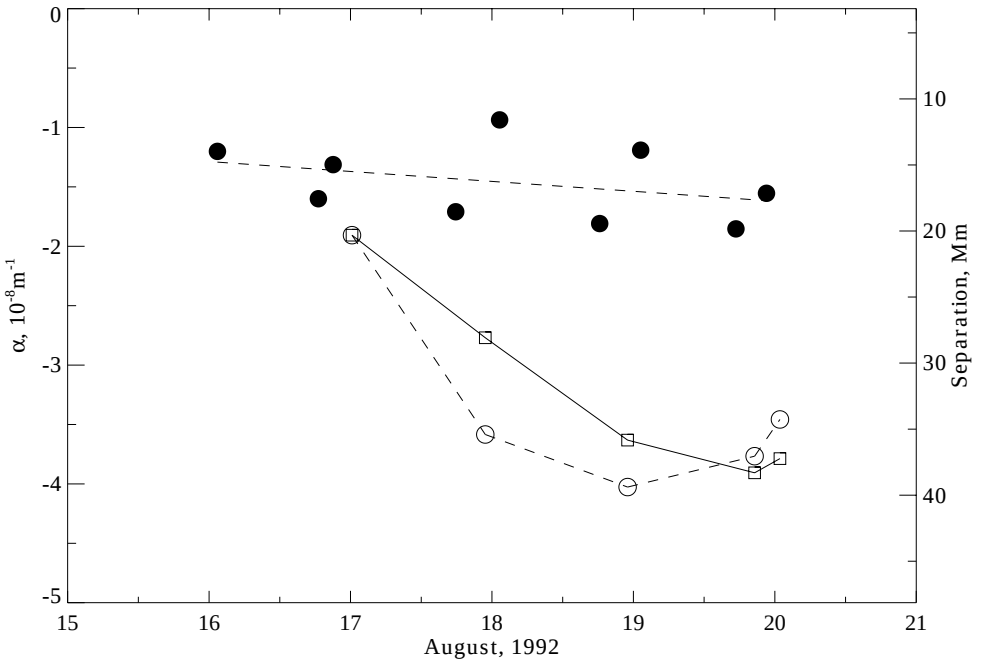

Fig. 6.— Evolution of an emerging region at the trailing portion of NOAA AR 7260. Circles indicate α_{best} measured from vector magnetograms. Filled circles are the existing region (the leading sunspot of NOAA AR 7260) and open circles are emerging portion. Squares show the polarity separation of the emerging section.

Table 1: Selected Active Regions.

NOAA	Date (beginning)	Latitude (deg)	CMD_B (deg)	CMD_E (deg)
8582	10-Jun-99	26.5	-50.6	-5.8
8738	20-Oct-99	18.7	-39.6	-13.1
8768	14-Nov-99	16.3	-57.7	-12.8
8817	3-Jan-00	25.7	-33.3	15.4
9139	19-Aug-00	9.9	-43.3	-5.4
9193	11-Oct-00	9.1	-4.7	25.5

Table 2: Fitted Model Parameters.

NOAA	$t_1 - t_0$	$\dot{d}$	d_0	$\bar{\alpha}$	ν	v_A	χ^2_ν
	days	m sec^{-1}	Mm	$10^{-8}\mathrm{m}^{-1}$	–	m sec^{-1}	–
8582	1.3	244±12	25.65	3.34±0.88	0.26±0.07	63±16	3.9
8738	...	...	...	0	...	...	...
8768	1.3	376±8	27.06	1.71±0.76	0.52±0.22	197±83	2.2
8817	1.0	229±9	26.79	2.17±0.27	0.41±0.05	94±11	8.2
9139	1.8	264±6	11.74	2.36±0.17	0.60±0.04	158±11	2.4
9193	1.0[†]	134±5	23.45	22.06±1.45	0.44±0.02	59±4	5.8

[†] t_0 and t_1 reflect phase of increasing α.

Table 3: Characteristics of AR emergence in our sample.

NOAA	Flux	Helicity	dH_R/dt
	10^{20} Mx	10^{41} Mx^2	10^{41} Mx^2/day
8582	30	4.0	2.3
8738	...	...	...
8768	13	1.3	1.4
8817	17	0.9	0.9
9139	44	12.7	1.6
9193	20	10	1.1